Article

Understanding Chromium Slag Recycling with Sintering–Ironmaking Processes: Influence of Cr_2O_3 on the Sinter Microstructure and Mechanical Properties of the Silico–Ferrite of Calcium and Aluminum (SFCA)

Ju Xu [1,2,3], Guojun Ma [1,2,3], Mengke Liu [1,2,3,*], Xiang Zhang [1,2,3], Dingli Zheng [1,2,3], Tianyu Du [1,2,3], Yanheng Luo [1,2,3] and Wei Zhang [1,2,3]

[1] The State Key Laboratory of Refractories and Metallurgy, Wuhan University of Science and Technology, Wuhan 430081, China; xuju@wust.edu.cn (J.X.); gma@wust.edu.cn (G.M.); zx91@wust.edu.cn (X.Z.); dinglizheng@wust.edu.cn (D.Z.); dty2021@wust.edu.cn (T.D.); 202102704170@wust.edu.cn (Y.L.); wei_zhang@wust.edu.cn (W.Z.)

[2] Joint International Research Laboratory of Refractories and Metallurgy, Ministry of Education, Wuhan University of Science and Technology, Wuhan 430081, China

[3] Key Laboratory for Ferrous Metallurgy and Resources Utilization of Ministry of Education, Wuhan University of Science and Technology, Wuhan 430081, China

* Correspondence: liumengke@wust.edu.cn; Tel.: +86-27-68862186; Fax: +86-27-68862529

Abstract: Chromium slag is a solid waste of chromium salt production, which contains highly toxic Cr(VI) and significant amounts of valuable metals, such as Fe and Cr. Recycling chromium slag as a raw sintering material in sintering–ironmaking processes can simultaneously reduce toxic Cr(VI) and recover valuable metals. A micro-sintering experiment, compressive strength test, microhardness test, and first-principles calculation are performed to investigate the influence of Cr_2O_3 on the sintering microstructure and mechanical properties of the silico-ferrite of calcium and aluminum (SFCA) in order to understand the basis of the sintering process with chromium slag addition. The results show that the microstructure of SFCA changes from blocky to interwoven, with further increasing Cr_2O_3 content from 0 wt% to 3 wt%, and transforms to blocky with Cr_2O_3 content increasing to 5 wt%. Cr_2O_3 reacts with Fe_2O_3 to form $(Fe_{1-x}Cr_x)_2O_3$ ($0 \leq x \leq 1$), which participates in forming SFCA. With the increase in Cr doping concentrations, the hardness of SFCA first decreases and then increases, and the toughness increases. When Cr_2O_3 content increases from 0 wt% to 3 wt%, the SFCA microhardness decreases and the compressive strength of the sintered sample increases. Further increasing Cr_2O_3 contents to 5 wt%, the SFCA microhardness increases, and the compressive strength of sintered sample decreases.

Keywords: Cr_2O_3; sinter; SFCA; first principles; mechanical property

1. Introduction

Chromium slag is a solid by-product of chromium salt manufacture in the chemical industry [1,2]. It is recognized as one of the hazardous solid wastes due to the fact that it contains harmful components, such as carcinogenic calcium chromate and highly toxic water-soluble Cr(VI) [3–5]. The accumulation and landfills of chromium slag, therefore, usually cause serious pollution to soil and groundwater, which severely endangers the ecological environment and human health [6,7]. It is estimated that the cumulative accumulation of chromium slag in China has exceeded 6 million tons [8,9].

At present, chromium slag is treated by reduction, stabilization, and comprehensive utilization processes around the world [10–14]. Within these treatment processes, secondary wastes are generated that cause environmental pollution. Simultaneously, the precious metals in chromium slag cannot be reused. Furthermore, the low utilization rate

of chromium slag is one of the reasons for the accumulation problem of chromium slag. The chemical composition of chromium slag is mainly composed of Fe_2O_3, Al_2O_3, SiO_2, Cr_2O_3, and MgO, which makes it similar to iron ore. Therefore, to improve the economic value and utilization efficiency of chromium slag, applying the chromium slag as a raw sintering material is a successful method. It can not only reduce Cr(VI) in chromium slag under a reducing atmosphere to realize the harmless utilization of chromium slag but also efficiently recover valuable metal components, such as Fe and Cr [15].

The sinter is an intermediate product that will eventually be used as a raw material in the blast furnace ironmaking process; hence, the operation of blast furnace smelting will depend on the quality of the sinter [16,17]. Previous studies demonstrated that adding chromium slag to the sintering raw materials deteriorated the tumble strength of the high-basicity sinter, which had a notable influence on the quality of the high-basicity sinter [18]. The drum strength of the sinter mainly depends on the microstructure of the sinter and the self-strength of the binder phase in the sinter. However, the silico-ferrite of calcium and aluminum (SFCA) is the primary bonding phase of the high-basicity sinter [19].

Several works found that Fe_2O_3, Al_2O_3, SiO_2, and MgO played a remarkable role in the mineral microstructure of the sinters and the mechanical properties of SFCA in sinters [20]. Gan et al. [21] and Higuchi et al. [22] found that the fraction of SFCA increased along with the amount of Al_2O_3 in the sinter, increasing the sinter's mechanical strength. When the Al_2O_3 content is above 1.8%, weak flake SFCA would form, reducing the mechanical strength of the sinter. Shi et al. [23] and Zhou et al. [24] found that with the increase in MgO content, the formation of $MgO \cdot Fe_2O_3$ by the reaction between MgO and Fe_2O_3 increased the formation temperature of the liquid phase in the sinter, resulting in a decrease in the liquid phase content and calcium ferrite mass fraction, which leads to a decrease in the strength of the sinter. Wang et al. [25,26] found that increasing the SiO_2 content in the sinter to 4 wt% promoted the formation of calcium ferrite. Further increasing the SiO_2 content caused the formation of silicate, which reduced the contact surface between CaO and Fe_2O_3, inhibited the formation of calcium ferrite, and reduced the strength of the sinter. Xue et al. [27,28] studied the influence and mechanism of basicity and temperature on the bonding phase strength (BS) and microstructure of high-chromium vanadium–titanium magnetite (HCVTM). The results showed that the BS of HCVTM sintered increased slightly with increasing temperature because the increase in temperature was beneficial to the formation of SFCA. Tu et al. [29] made composite pellets of chromium slag and carbon-containing dust for co-sintering with limonitic laterite. The results showed that the addition of more than 20% of chromium slag destroyed the drum strength of the sinter. Cr(III) mainly existed in spinel and SFCA. However, the effect of Cr_2O_3 content on the microstructure of the sinter, as well as the self-strength of SFCA, has not been reported yet.

The advancement of simulation technology in recent years has promoted the research of material toughening and strengthening mechanisms at the microscale and created a connection between theory and experiment [30]. The first-principles approach involves analyzing the properties of materials at the molecular and electron level, such as mechanical properties and electronic structure, thereby enabling the prediction of material performance to a certain extent [31]. In the field of materials, first principles have been widely used to predict the properties of iron, steel, and alloys [32]. First-principles calculations can provide theoretical guidance for alloy composition design [33]. This research method holds significant potential for practical applications in the steel industry. Therefore, it is beneficial to analyze the mechanical properties of SFCA at the microlevel by applying the first-principles calculation method. First-principles calculations can be used to determine the bulk modulus, shear modulus, Young's modulus, Poisson's, and Pugh's modulus ratios of SFCA crystals. These parameters can predict the strength and toughness of SFCA. Yang et al. [34] investigated the impact of Al doping on the mechanical properties of calcium ferrite crystal via first-principles calculations. The results demonstrated that Al doping can increase the crystal strength of calcium ferrite.

In this work, the effects of Cr_2O_3 on the strength of sinters and the microhardness of SFCA in sinters were investigated via compressive strength and microhardness tests. The composition and morphology of the phases in the sinter were detected via X-ray diffraction (XRD) and scanning electron microscopy using an energy-dispersive spectrometer (SEM-EDS). The influence of Cr doping on the mechanical properties of SFCA was revealed via first-principles calculation. The aim of this study is to provide theoretical guidance and an experimental basis for the utilization of chromium slag in the sintering process.

2. Results and Discussion

2.1. Mineral Composition and Microstructure of the Sinter

2.1.1. Mineral Composition of the Sinter

Figure 1 displays the XRD patterns of sinters with different Cr_2O_3 contents. It can be seen that the main phases in the specimens are hematite (Fe_2O_3), the silico-ferrite of calcium and aluminum (SFCA), and silicate. When the Cr_2O_3 content in sinters increases to 1 wt%, the diffraction peaks corresponding to $(Fe_{1-x}Cr_x)_2O_3$ ($0 \leq x \leq 1$) can be observed in the XRD pattern, and the intensity increases with the increase in Cr_2O_3 content. Figure 2 indicates the crystal structures of Fe_2O_3, Cr_2O_3, and $(Fe_{1-x}Cr_x)_2O_3$. It is clear that the crystal structures of Fe_2O_3 and Cr_2O_3 both belong to the monoclinic crystal system. The ionic radii of Fe and Cr are 0.55 Å and 0.62 Å, respectively. The insignificant difference between these ionic radii provides the conditions for Fe_2O_3 and Cr_2O_3 to form continuous solid solutions [35]. Therefore, Cr on the surface of hematite Fe_2O_3 easily migrates into the lattice of Fe_2O_3 by diffusion, replaces Fe, and occupies the iron ion vacancies in the hematite lattice forming $(Fe_{1-x}Cr_x)_2O_3$.
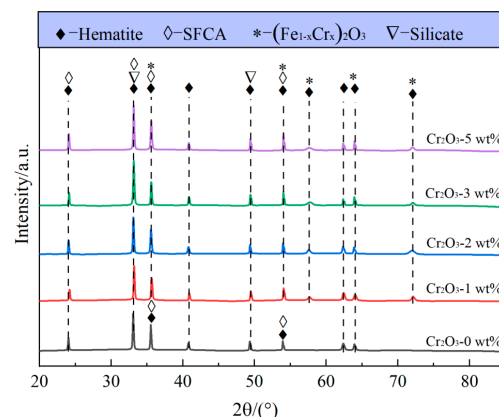
Figure 1. XRD patterns of samples with different Cr_2O_3 contents.
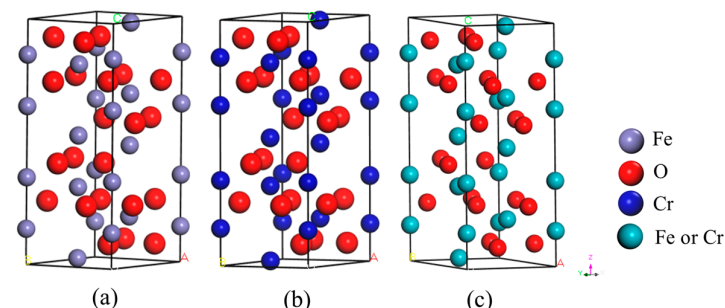
Figure 2. Crystal structures of Fe_2O_3, Cr_2O_3 and $(Fe_{1-x}Cr_x)_2O_3$: (**a**) Fe_2O_3; (**b**) Cr_2O_3; (**c**) $(Fe_{1-x}Cr_x)_2O_3$.

2.1.2. Microstructure of Sinters

To reveal the influence of Cr_2O_3 on the microstructure of sinters, SEM-EDS was used to characterize the morphology and composition of phases in sintered samples. The results

are shown in Figure 3 and Table 1, respectively. The sintered samples were discovered to include four phases, as demonstrated in the SEM results. These phases, when paired with the EDS analysis (Table 1), were identified as hematite, SFCA, silicate, and $(Fe_{1-x}Cr_x)_2O_3$, which is compatible with the XRD results (Figure 1).
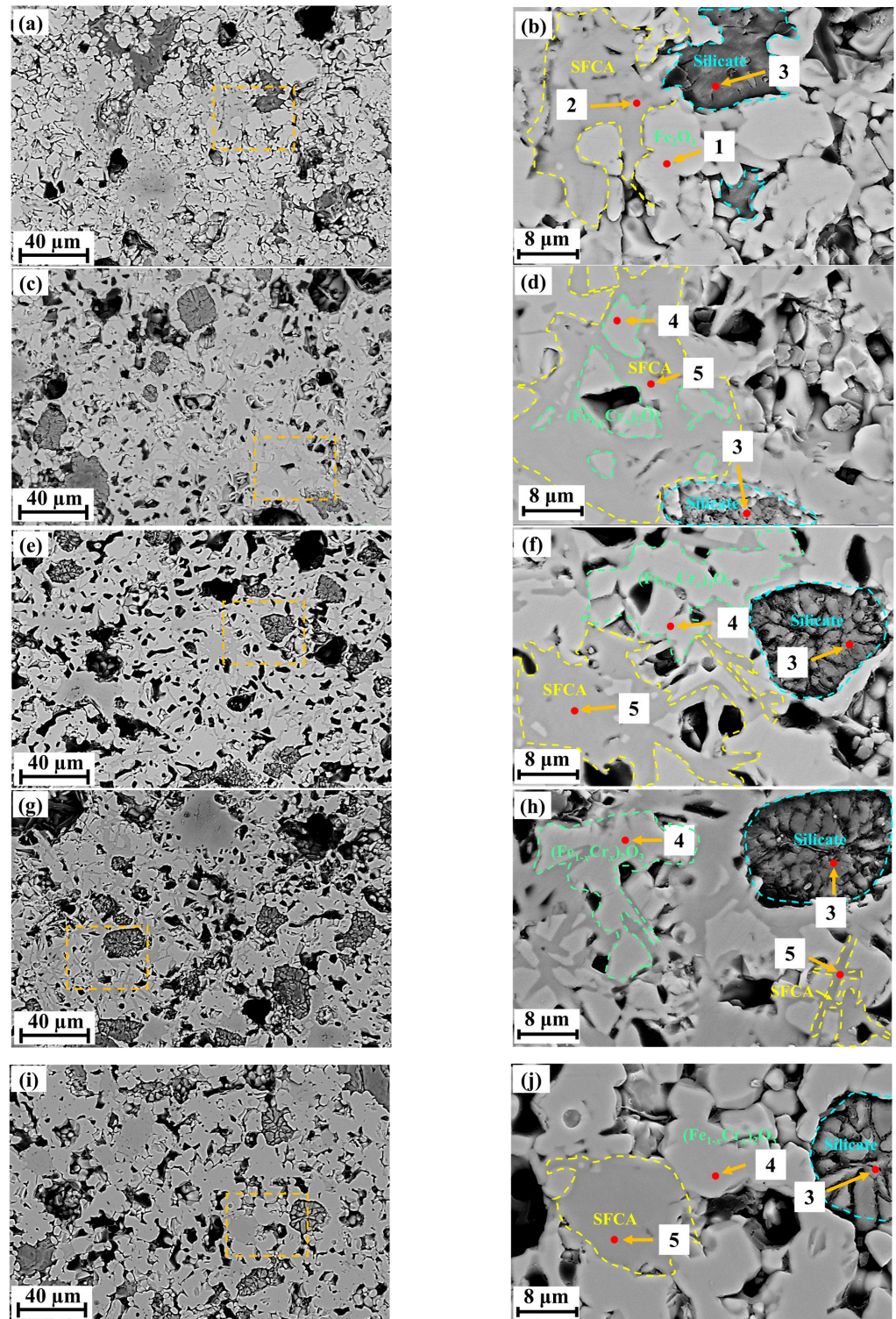
Figure 3. SEM results of samples with different Cr_2O_3 content. (**a,b**): 0 wt% Cr_2O_3; (**c,d**): 1 wt% Cr_2O_3; (**e,f**): 2 wt% Cr_2O_3; (**g,h**): 3 wt% Cr_2O_3; (**i,j**): 5 wt% Cr_2O_3; (**b,d,f,h,j**) are enlarged images of the enclosed areas of (**a,c,e,g,i**), respectively.

**Table 1.** Element content of sintered samples (at.%).

Location	Point	Fe	O	Ca	Si	Al	Cr	Phase
	1	50.5	49.5	-	-	-	-	Hematite
5b	2	31.0	54.0	8.4	3.1	3.5	-	SFCA
	3	-	58.6	20.8	20.5	-	-	Silicate
	4	53.1	45.9	-	-	-	1.0	$(Fe_{1-x}Cr_x)_2O_3$
5d	5	38.5	44.8	9.7	3.8	2.6	0.6	SFCA
	3	-	56.1	22.6	21.6	-	-	Silicate
	4	51.0	47.5	-	-	-	1.6	$(Fe_{1-x}Cr_x)_2O_3$
5f	5	42.9	49.7	4.4	1.6	2.0	0.9	SFCA
	3	-	58.5	27.0	13.7	-	-	Silicate
	4	49.3	48.5	-	-	-	2.2	$(Fe_{1-x}Cr_x)_2O_3$
5h	5	35.5	50.7	8.6	2.5	1.0	1.4	SFCA
	3	-	56.0	29.3	14.7	-	-	Silicate
	4	49.7	47.1	-	-	-	3.2	$(Fe_{1-x}Cr_x)_2O_3$
5j	5	41.1	46.6	5.0	2.7	2.5	2.7	SFCA
	3	-	67.6	21.0	11.4	-	-	Silicate

Figure 3 exhibits the SEM results of sintered samples with different Cr_2O_3 contents. As is verified in Figure 3a,b, the dominant phases are hematite with an irregular shape, blocky SFCA, and massive silicate bonding hematite. The SFCA is unevenly distributed, and its size is large. When Cr_2O_3 content increases to 1.0 wt%, the dominant phase in the sintered sample is irregularly shaped $(Fe_{1-x}Cr_x)_2O_3$, and an interwoven SFCA appears, which is presented in Figure 3c,d. The distribution of interwoven SFCA is more uniform, while the content of plate SFCA is lower. When the content of Cr_2O_3 increases to 2.0 wt% and 3.0 wt%, the main phase in sintered samples is $(Fe_{1-x}Cr_x)_2O_3$, which is bonded by interwoven SFCA and massive silicate, as presented in Figure 3e,f and Figure 3g,h, respectively. The interwoven SFCA content gradually increases. Increasing the Cr_2O_3 content to 5.0 wt%, $(Fe_{1-x}Cr_x)_2O_3$ is the dominant phase, which is illustrated in Figure 3i,j. SFCA is shown as a block and its content decreases; the microstructure of the silicate phase remains constant, but its content increases.

It can be seen from the EDS results in Table 1 that in the sintered samples without Cr_2O_3, the hematite consists of Fe and O elements and the SFCA consists of Fe, Ca, Si, Al, and O elements. From the EDS results of point 4 in Figure 3d,f,h,j, a new phase can be observed in the sintered samples containing Cr_2O_3 and is identified to be $(Fe_{1-x}Cr_x)_2O_3$ which is composed of Fe, O, and Cr elements. All SFCA in the sintered samples containing Cr_2O_3 contain a small amount of Cr. Moreover, the atomic ratio of the Cr element in $(Fe_{1-x}Cr_x)_2O_3$ and SFCA increases with an increase in Cr_2O_3 content in sintered samples. This indicates that Cr elements participate in the formation of $(Fe_{1-x}Cr_x)_2O_3$ and SCFA during the sintering process.

The reaction mechanism is schematically depicted in Figure 4. Fe_2O_3 and Cr_2O_3, shown in the marked red region in Figure 4a, react to form $(Fe_{1-x}Cr_x)_2O_3$, which is displayed as the red phase in Figure 4b. SiO_2 and CaO in the sinter (in the marked green region in Figure 4b) react to form silicate. The formed silicate presents as the green phase in Figure 4c, which is the generation of silicate observed via SEM-EDS. In the sintered sample, $(Fe_{1-x}Cr_x)_2O_3$ reacts with SiO_2, Al_2O_3, and CaO to form Cr-containing SFCA, which exhibits the blue phase in Figure 4c. Therefore, some amounts of Cr elements are found in the SFCA in the sintered samples with Cr_2O_3. The formation temperature of $(Fe_{1-x}Cr_x)_2O_3$ is about 500 °C, while the formation temperature of SFCA is 1107 °C–1164 °C [36]. $(Fe_{1-x}Cr_x)_2O_3$ is formed first during the sintering process, and then the formed $(Fe_{1-x}Cr_x)_2O_3$ reacts with CaO, SiO_2, and Al_2O_3 to generate the SFCA.
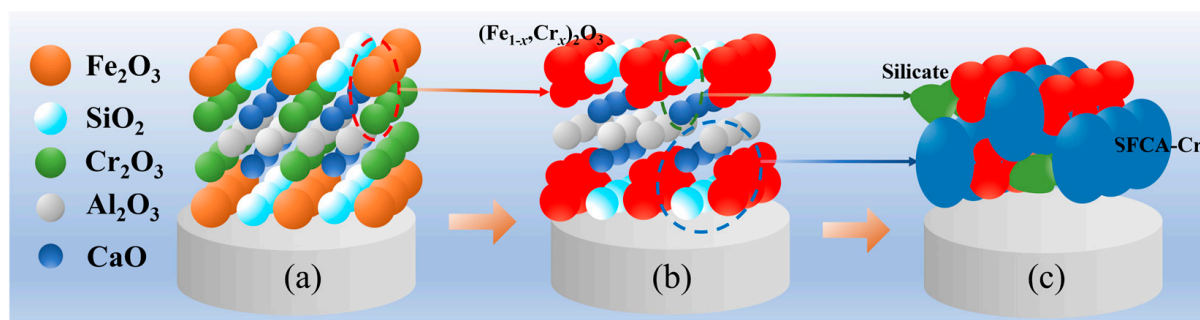
Figure 4. Formation mechanism of SFCA with Cr.

2.2. Mineral Composition of Sinter

The aforementioned results found that with the increase in Cr_2O_3 content in the sintered samples, Cr atoms were gradually doped into SFCA crystals, which could affect the mechanical properties of SFCA and thus the metallurgical quality of the sinter ore. Therefore, the first-principles calculation was conducted to reveal the influencing mechanism of Cr doping into SFCA crystals on the mechanical properties of SFCA crystals. First, the crystal structure of SFCA crystals with and without Cr doping was geometrically optimized via the quantum mechanics program CASTEP [37]. Then, the elastic constants were calculated via the stress–strain method based on the optimized structure.

Table 2 lists the calculated lattice constants of SFCA crystals with different amounts of Cr doping. It can be found that adding Cr to SFCA crystals results in obvious lattice deformation. Furthermore, with an increase in doped Cr concentrations, the cell volume rises while the lattice remains unchanged. The radii of Fe and Cr atoms are 1.56 Å and 1.66 Å, respectively, while the radii of their covalent bonds are 1.16 Å and 1.22 Å, respectively. When Cr atoms replace Fe atoms, the small atomic radii are replaced by large atomic radii. Simultaneously, the small covalent bond radii are replaced by a large covalent bond radius, so the volume of SFCA crystals increases with the increase in the amount of Cr atoms.

Table 2. Lattice parameters of SFCA crystals.

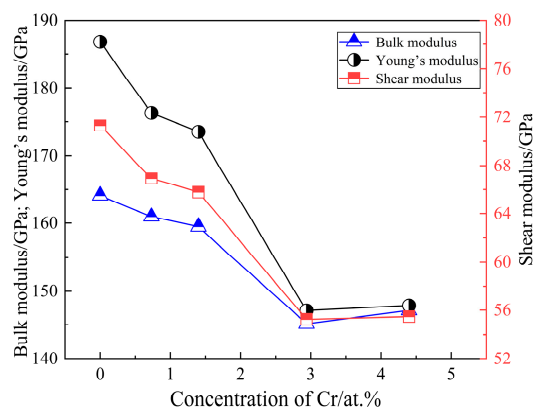| Doped Cr Concentrations	a/Å	b/Å	c/Å	α/(°)	β/(°)	γ/(°)	V/Å^3
0 at.%	8.824	9.830	10.560	60.157	74.223	66.567	726.213
0.73 at.%	17.656 *	9.816	10.578	60.229	74.16	66.68	1454.73 *
1.4 at.%	8.819	9.809	10.591	60.317	74.215	66.678	727.921
2.94 at.%	8.754	9.892	10.741	59.313	74.00	66.415	730.033
4.4 at.%	8.764	9.859	10.732	59.755	73.788	66.764	732.551

*: It should be noted that the lattice constant "a" with a Cr doping amount of 0.73 at% is larger because the SFCA crystal builds up $2 \times 1 \times 1$ supercells during calculations.

To investigate the effect of doped Cr concentrations on the mechanical properties of SFCA crystals, the bulk modulus and shear modulus of SFCA crystals with different doped Cr concentrations are analyzed. To ensure that the calculated data are valid, the stability of the crystal mechanics of Cr-doped SFCA crystals should be investigated before considering the elastic property. The elastic constants of these structures satisfy the Born stability criterion for trigonal crystalline systems [38,39]. The sixth-order symmetric matrix C must be positive definite, meaning that all primary determinants must be greater than zero, as this is a sufficient condition for the stability of the triclinic system. The calculated elastic constants of SFCA crystals with different doped Cr concentrations are listed in Table 3. This indicates that the SFCA crystals with doped Cr concentrations from 0 at.% to 4.4 at.% are elastically stable.

Table 3. Elastic constants of SFCA crystals with different doped Cr concentrations (GPa).

Cij	0 at.%	0.73 at.%	1.4 at.%	2.94 at.%	4.4 at.%
C11	256.568	257.856	245.337	223.854	211.351
C22	270.272	268.028	263.525	218.938	230.516
C33	241.514	227.568	235.047	227.912	227.579
C44	77.589	66.428	61.900	55.212	59.503
C55	71.859	68.499	70.849	54.912	48.917
C66	75.784	68.652	69.669	50.645	58.813
C12	137.168	129.89	128.352	104.603	106.489
C13	108.344	111.985	111.342	104.872	110.914
C14	7.399	6.114	0.361	6.397	1.088
C15	−4.516	−3.137	−5.609	−5.878	−9.866
C16	−9.782	−1.456	−6.548	−9.726	−10.157
C23	116.799	110.810	112.913	109.953	114.901
C24	−7.115	−4.727	−15.987	3.942	−5.904
C25	4.668	7.505	5.113	−0.783	−6.277
C26	−24.12	14.140	−20.712	1.803	−4.272
C34	−1.612	−2.667	−8.373	0.779	−8.557
C35	−2.660	−4.662	−2.214	−0.390	−3.566
C36	−7.844	−5.225	−3.955	−3.450	−4.281
C45	−2.177	−1.191	−1.576	0.923	3.262
C46	1.519	4.522	3.213	1.010	−0.159
C56	3.151	0.641	−0.125	−0.912	0.663

Figure 5 illustrates the calculated results of the bulk modulus, shear modulus, and Young's modulus of SFCA crystals with different doped Cr concentrations. The bulk modulus, shear modulus, and Young's modulus of SFCA crystals decreased initially and subsequently increased when the Cr doping concentration rose from 0 at.% to 4.4 at.%. The bulk modulus, shear modulus, and Young's modulus of SFCA crystal decrease from 164.112 GPa to 145.139 GPa, 71.276 GPa to 55.247 GPa, and 186.786 GPa to 147.079 GPa, with increasing Cr doping concentrations from 0 at.% to 2.94 at.%, respectively. The bulk modulus, shear modulus, and Young's modulus of SFCA crystals increase to 147.097 GPa, 55.464 GPa, and 147.814 GPa with a further increase in Cr doping concentrations to 4.4 at.%, respectively.

Figure 5. Bulk modulus, shear modulus, and Young's modulus for SFCA crystals with different doped Cr concentrations.

There exists a monotonic relationship between the hardness of SFCA and the elastic constant C44: the higher the C44, the greater the hardness of SFCA [40]. As listed in Table 3, C44 exhibits a decreasing trend followed by an increasing trend. As the Cr doping concentration increases from 0 at.% to 2.94 at.%, the value of C44 decreases from 77.589 GPa to 55.212 GPa. Similarly, as the Cr doping concentration increases from 2.94 at.% to 4.4 at.%, the value of C44 increases from 55.212 GPa to 59.503 GPa.

The variation in hardness is the result of the combined effects of multiple factors, including atomic radius, interatomic charge density, and lattice defects [41]. It can be seen from Table 2 that the atomic radius of Cr is larger than that of Fe, which leads to the expansion of the lattice volume of the SFCA crystal when Cr atoms replace Fe atoms, resulting in internal defects that reduce the mechanical properties of crystals [42,43]. Furthermore, doping can change the electron density and impact the strength of atom bonds, resulting in various mechanical characteristics [40]. The electron density distribution and density of states of SFCA crystals doped with different doped Cr concentrations are indicated in Figure 6. It can be seen from Figure 6a that the electron density distributed between Cr and O atoms increases as the doping amount of Cr atoms increases. The doping of Cr atoms causes a considerable buildup of overlapping electrons between the Cr and O atoms, resulting in the formation of potent covalent bonds that increase crystal hardness. Meanwhile, in the interval from −9 to 3 eV, the d orbital of Fe, the p orbital of O, and the d orbitals of Cr generate strong hybridization, as depicted in Figure 6b. The hybridization of electrons is the main factor that distinguishes the hardness of materials and can be used to obtain the hardness enhancement of the SFCA crystals after Cr doping. Hence, when the doping concentration of Cr is within the range of 0–2.94 at.%, the increase in lattice volume, which results in severe internal defects, is the primary reason for the drop in the hardness of SFCA crystals. However, as the Cr doping concentration increases to 4.4 at.%, more Cr atoms participate in strong covalent interactions with O atoms, increasing the crystal's hardness. Therefore, from any perspective, it can be concluded that the hardness of SFCA decreases as the doping concentration of Cr increases from 0 at.% to 2.94 at.% and then increases as the doping concentration of Cr increases from 2.94 at.% to 4.4 at.%.
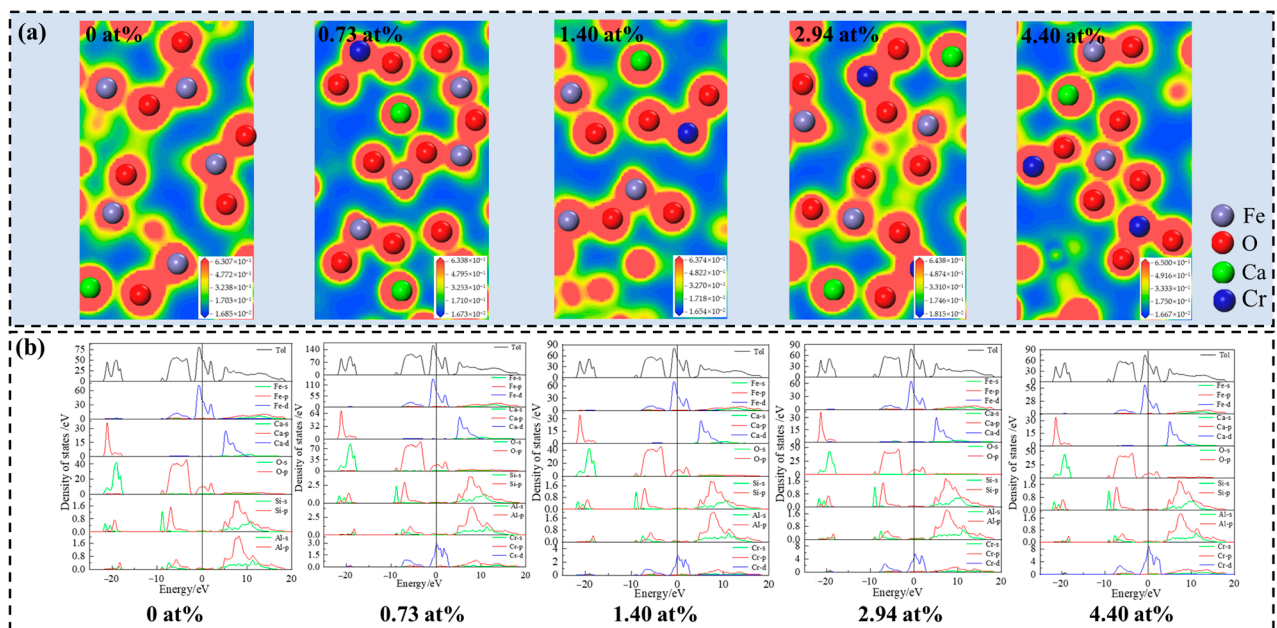
Figure 6. (**a**) The electron density distribution of SFCA crystals doped with different doped Cr concentrations; (**b**) the density of states of SFCA crystals doped with different doped Cr concentrations.

Pugh's modulus ratio G/B and Poisson's ratio υ are important parameters for evaluating the toughness and brittleness of materials. A larger value of G/B indicates the increased brittleness of the material with a critical value of 0.571, while a larger Poisson's ratio indicates a material with better toughness [44,45]. Figure 7 reveals the calculated results of the Pugh modulus ratio G/B and Poisson's ratio υ of SFCA crystals with various doped Cr concentrations. It is clear that all G/B values of SFCA crystals with various doped Cr concentrations are less than 0.571, indicating that the crystal structure is ductile both before and after doping. When the doped Cr concentration increases from 0 at.% to

4.4 at.%, the G/B value decreases from 0.434 to 0.381, and Poisson's ratio increases from 0.310 to 0.331. This demonstrates that the addition of Cr can enhance the toughness of SFCA crystals. SFCA with better toughness can absorb more energy from the impact or dynamic load, which can bear larger deformations.
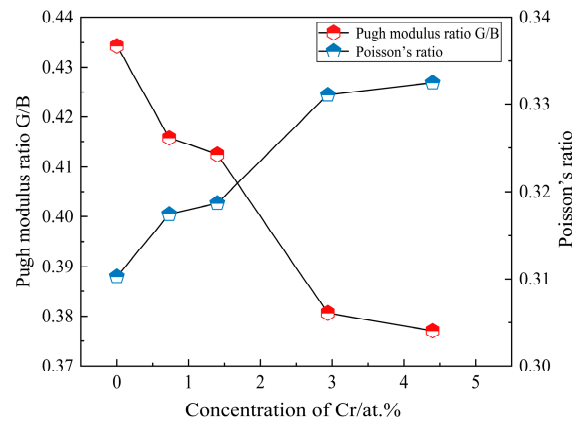

Figure 7. G/B values and Poisson's ratio for SFCA crystals doping with different Cr concentrations.

2.3. Mineral Composition and Microstructure of the Sinter

2.3.1. Effect of Cr_2O_3 on Microhardness of SFCA

Figure 8 displays the effect of Cr_2O_3 content on the microhardness of SFCA. It can be observed from Figure 8 that with the increase in Cr_2O_3 content, the microhardness of SFCA shows a trend of first decreasing and then increasing. When the Cr_2O_3 content increases from 0 wt% to 3 wt%, the microhardness of SFCA decreases from 738.94 HV0.05 to 626.67 HV0.05. With a further increase in the Cr_2O_3 content to 5 wt%, the microhardness of SFCA increases to 753.77 HV0.05.
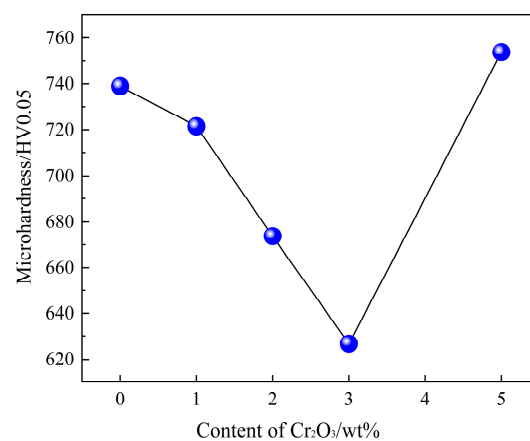
**Figure 8.** Effect of Cr_2O_3 content on microhardness of SFCA.

The mechanical properties of materials exhibit a certain connection at both the microscopic and macroscopic levels. On the macroscopic scale, the material's microhardness is directly proportional to the microscopic aspects of the crystal's bulk modulus, shear modulus, and Young's modulus [46]. According to first-principles calculations, it was observed that the hardness of SFCA crystals decreased, and toughness increased as the Cr doping concentration escalated from 0% to 2.94%. Conversely, an increase in Cr doping concentration from 2.94% to 4.4% resulted in an elevation in the hardness of SFCA crystals and a decrease in toughness. These align with the experimental results obtained from microhardness tests conducted on the SFCA phase in the samples. The first-principles simulation lacks consideration of the simultaneous substitution of Fe and Al atoms for Cr atoms. However, this represents a noteworthy aspect that will be subjected to a more

comprehensive study in the future. The forthcoming research aims to provide a deeper understanding of the atomic interactions and behaviors within the system under investigation, with a focus on elucidating the effects of the substitution process on the properties of the material.

2.3.2. Effect of Cr_2O_3 on the Compressive Strength of Sinter

Figure 9 indicates the effect of Cr_2O_3 content on the compressive strength of the sinter. It is clear in Figure 9 that the compressive strength of the sinter without Cr_2O_3 addition is 16.2 MPa. When the Cr_2O_3 content increases to 3 wt%, the compressive strength of the sample increases to 106.2 MPa. While the compressive strength of sintered samples decreases to 72.9 MPa with a further increase in Cr_2O_3 content to 5 wt%. The results demonstrate that adding Cr_2O_3 can improve the compressive strength of the sintered sample, and excessive Cr_2O_3 deteriorates the compressive strength of the sintered sample.
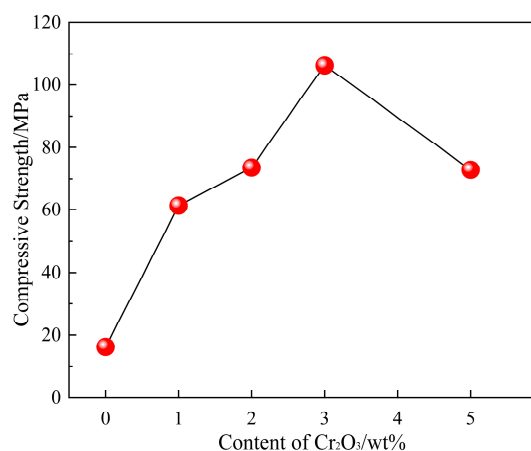
Figure 9. Effect of Cr_2O_3 content on the compressive strength of the sinter.

Many factors affect the strength of sintered samples, such as the strength and structure of SFCA and the formation of the liquid phase in sintered samples. Although the microhardness of SFCA in sintered samples decreases with an increase in Cr_2O_3 content, the formation of more interwoven SFCA can effectively inhibit crack propagation, which makes the compressive strength of interwoven SFCA better than that of a single blocky SFCA and enhances the compressive strength of sintered samples [20,47,48]. When Cr_2O_3 content increases to 5 wt%, more Cr participates in Fe_2O_3, which enhances the stability of $(Fe_{1-x}Cr_x)_2O_3$. It inhibits the reaction between $(Fe_{1-x}Cr_x)_2O_3$ and CaO, Al_2O_3, and SiO_2 to form SFCA and leads to a reduction in the amount of liquid phase in sintered samples, which results in a decrease in the compressive strength of the sinter ore.

3. Experimental Section

3.1. Sample Preparation

In order to eliminate the impact of minor components in chromium slag, analytical grades of (AR) Fe_2O_3 ($\geq$99.9 wt%), SiO_2 ($\geq$99.9 wt%), Al_2O_3 ($\geq$99.9 wt%), CaO ($\geq$96.0 wt%), and Cr_2O_3 ($\geq$99.9 wt%) were used as raw materials to generate experimental sintered samples. The raw material ratios in this experiment were designed based on the basicity and composition of the sintered ore when chromium slag was used as a partially sintering raw material, and the basicity R (CaO/SiO_2) of the sintered ore was designed to be 1.8 [49]. The Cr_2O_3 contents were 0 wt%, 1 wt%, 2 wt%, 3 wt%, and 5 wt%, respectively, and the mass ratio of other components maintained constant. The chemical compositions of the samples are listed in Table 4.

Table 4. Chemical compositions of the studied sintered samples (wt%).

Samples	Fe$_2$O$_3$	Al$_2$O$_3$	CaO	SiO$_2$	Cr$_2$O$_3$
S1	81.38	2.13	10.57	5.94	0
S2	80.57	2.11	10.49	5.83	1
S3	79.76	2.09	10.38	5.77	2
S4	78.97	2.07	10.26	5.70	3
S5	78.18	2.05	9.50	5.28	5

According to the designed chemical compositions of the sintered samples, as depicted in Table 4, the raw materials were mixed with anhydrous ethanol for 30 min and dried at 100 °C for 2 h. The dried raw materials are ground and mixed thoroughly in an agate mortar. Then, about 1.5 g of raw material was pressed in a cylindric mold with the size of Φ10 mm × 6 mm under the pressure of 5.0 MPa and held for 2 min. To simulate the sintering process, the cylindric samples were maintained at 1200 °C for 10 h in the electric resistance furnace under an air atmosphere and then cooled to room temperature in the furnace. The process schematic of sample preparation and sintering is illustrated in Figure 10.
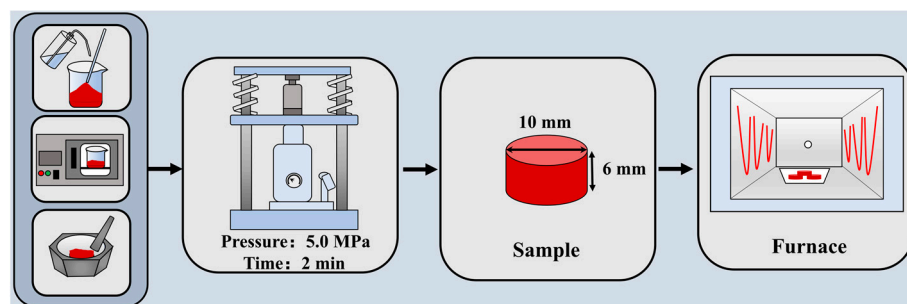
Figure 10. Process schematic of sample preparation and sintering.

3.2. Characterization of Sintered Samples

The sintered samples were ground into powders to determine the crystalline phases via XRD with Cu-Kα radiation (X'Pert PRO MPD, PANalytical, Almelo, The Netherlands). Parts of the sintered samples were inlaid with epoxy resin and polished, followed by coating a thin gold film onto the polished sample to enhance the electric conductivity of the sample. The microhardness of the SFCA phase in each sample was measured using an image-processing microhardness tester (HV-1000A, Shen Youda industrial, Shanghai, China). The morphology and chemical composition of phases in the sintered samples were identified via SEM-EDS (Nova NanoSEM400, FEI Hillsboro USA, EVO 010, Zeiss, X-MaxN 79416, Oxford UK). The compressive strength of samples was tested by a flexural and compressive testing machine (SJY-II, Xiangtan Instrument, Xiangtan, China), and the compressive strength was the average value of ten tests.

3.3. Method and Model of First-Principles Calculation

Based on the density functional theory (DFT), the calculations were performed using the CASTEP quantum mechanics module in the Materials Studio software. As Fe and Cr elements are both transition metal elements, their spin polarization was considered in the calculations. The valence electron configurations of Fe, Ca, Cr, O, Si, and Al in SFCA are $3d^6 4s^2$, $4s^2$, $3d^5 4s^1$, $2s^2 2p^4$, $3s^2 3p^2$, and $3s^2 3p$, respectively. The generalized gradient approximation (GGA) was employed to optimize SFCA cells and calculate the elastic modulus. The PBE generalized function was chosen for the electron correlation. The plane wave phase energy and k-point grid were chosen to be 450 eV and [2 × 2 × 2], respectively. The wave phase energy and k-point grid of 2 × 1 × 1 supercell was chosen to be 450 eV and [2 × 2 × 1], respectively.

To investigate the effect of Cr doping on the mechanical properties of SFCA crystals, a certain concentration of Fe atoms in the SFCA crystals was randomly replaced with Cr atoms. The elastic modulus of different crystals was calculated via the CASTEP module. The bulk modulus and shear modulus of crystals were calculated using the Voigt–Reuss–Hill method. The Young's modulus and Poisson's ratio of crystals were calculated using Equations (1) and (2) [50–52]. Among them, the bulk modulus represents the resistance of the material to external homogeneous compression in the elastic regime. The shear modulus is the ratio of shear stress to shear strain, which characterizes the ability of material to resist the shear strain. Young's modulus characterizes the ability of a solid material to resist deformation:

$$E = \frac{9B \times G}{3B + G} \tag{1}$$

$$v = \frac{3B - 2G}{2(3B + G)} \tag{2}$$

where B is the crystal bulk modulus, GPa; G is the shear modulus, GPa; E is Young's modulus, GPa; and v is Poisson's ratio.

The crystal structure of SFCA was determined via the XRD results of sintered samples. The SFCA crystal [53] belongs to the trigonal crystal system with space group P-1, and each cell contained 18 Fe atoms, 6 Ca atoms, 2 Al atoms, 2 Si atoms, and 40 O atoms, as presented in Figure 11a. Figure 11b–e display the SFCA cells with doped Cr concentrations of 0.73 at.%, 1.4 at.%, 2.94 at.%, and 4.4 at.%, respectively. In order to accommodate the Cr doping concentration of 0.73 at.% in the SFCA cell, a $2 \times 1 \times 1$ supercell needs to be created, as presented in Figure 11b. As the proportion of chromium atoms to all atoms in the crystal cell, the doped chromium concentration is calculated.
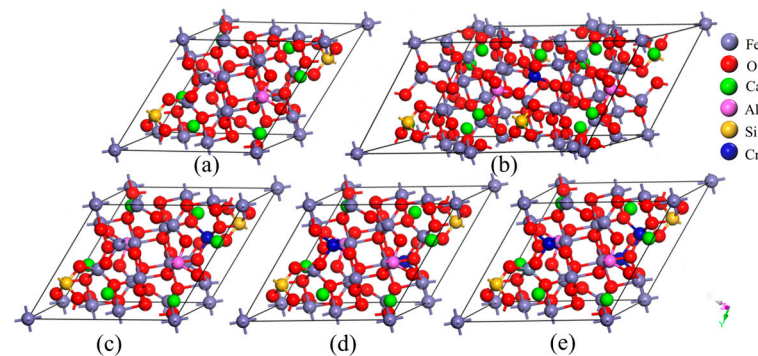
Figure 11. SFCA cells with different Cr doping amounts: (**a**) 0 at.%; (**b**) 0.73 at.%; (**c**) 1.40 at.%; (**d**) 2.94 at.%; (**e**) 4.40 at.%.

4. Conclusions

(1) The phases are Fe_2O_3, SFCA, and silicate in the sintered sample without Cr_2O_3. After adding Cr_2O_3 content ($\leq$5 wt%) in sintered samples, $(Fe_{1-x}Cr_x)_2O_3$ is found, which results from the doping of Cr into Fe_2O_3. Furthermore, the Cr element is also found in the SFCA. With the addition of Cr_2O_3, the contents of Cr in $(Fe_{1-x}Cr_x)_2O_3$ and SFCA increase.

(2) The microstructure of the SFCA in sinters changes from being blocky to being interwoven, with an increase in the content of Cr_2O_3 from 0 wt% to 3 wt%, and then it transforms to being blocky with a further increase in the content of Cr_2O_3 to 5 wt%.

(3) When the doping concentration of Cr increases from 0 at.% to 4.4 at.%, the SFCA cell volume increases. The bulk modulus, shear modulus, and Young's modulus decrease first and subsequently increase with the doping concentration of Cr, Pugh's modulus ratio G/B decreases, and Poisson's ratio increases. This demonstrates that the hardness of SFCA decreases as the doping concentration of Cr increases from 0 at.% to 2.94 at.%, and then it increases as the doping concentration of Cr increases from 2.94 at.% to 4.4 at.%. The toughness of SFCA increases with an increase in Cr doping concentrations.

(4) The microhardness of SFCA in sinters decreases from 738.94 HV0.05 to 626.67 HV0.05 with an increase in Cr_2O_3 content from 0 wt% to 3 wt%. The microhardness of SFCA increases to 753.77 HV0.05 with a further increase in the Cr_2O_3 content to 5 wt%. The variation in the microhardness of SFCA is consistent with the trend of first-principles calculations.

(5) The compressive strength of sintered samples increases from 12.6 MPa to 106.2 MPa with an increase in the content of Cr_2O_3 from 0 wt% to 3 wt% and then decreases to 72.9 MPa with a further increase in the content of Cr_2O_3 to 5 wt%.

References

1. Peng, Z.W.; Wang, L.C.; Gu, F.Q.; Tang, H.M.; Rao, M.J.; Zhang, Y.B.; Li, G.H.; Jiang, T. Recovery of chromium from ferronickel slag: A comparison of microwave roasting and conventional roasting strategies. *Powder Technol.* **2020**, *372*, 578–584. [CrossRef]
2. Zhao, G.Z.; Zhang, L.L.; Cang, D.Q. Pilot trial of detoxification of chromium slag in cyclone furnace and production of slag wool fibres. *J. Hazard. Mater.* **2018**, *358*, 122–128. [CrossRef] [PubMed]
3. Chai, L.Y.; Huang, S.H.; Yang, Z.H.; Peng, B.; Huang, Y.; Chen, Y.H. Cr (VI) remediation by indigenous bacteria in soils contaminated by chromium-containing slag. *J. Hazard. Mater.* **2009**, *167*, 516–522. [CrossRef]
4. Jagupilla, S.C.; Moon, D.H.; Wazne, M.; Christodoulatos, C.; Min, G.K. Effects of particle size and acid addition on the remediation of chromite ore processing residue using ferrous sulfate. *J. Hazard. Mater.* **2009**, *168*, 121–128. [CrossRef] [PubMed]
5. Wu, J.N.; Li, C.L.; Yang, F. The disposition of chromite ore processing residue (COPR) incorporating industrial symbiosis. *J. Clean. Prod.* **2015**, *95*, 156–162. [CrossRef]
6. Li, Y.M.; Li, Q.; Yang, F.Y.; Bao, J.; Hu, Z.H.; Zhu, W.W.; Zhao, Y.Y.; Lin, Z.D.; Dong, Q.S. Chromium (VI) detoxification by oxidation and flocculation of exopolysaccharides from *Arthrobacter* sp. B4. *J. Biol. Macromol.* **2015**, *81*, 235–240. [CrossRef] [PubMed]
7. Wu, S.L.; Hu, Y.J.; Zhang, X.; Sun, Y.Q.; Wu, Z.X.; Li, T.; Lv, J.T.; Li, J.L.; Zhang, J.; Zheng, L.R. Chromium detoxification in arbuscular mycorrhizal symbiosis mediated by sulfur uptake and metabolism. *Environ. Exp. Bot.* **2018**, *147*, 43–52. [CrossRef]
8. Wei, Y.F.; Wang, J.; Wang, J.X.; Zhan, L.; Ye, X.; Tan, H.B. Hydrothermal processing, characterization and leaching toxicity of Cr-added "fly ash-metakaolin" based geopolymer. *Constr. Build. Mater.* **2020**, *251*, 118931. [CrossRef]
9. Chen, J.Y.; Wang, Y.H.; Zhou, S.; Lei, X.R. Reduction/immobilization processes of hexavalent chromium using metakaolin-based geopolymer. *J. Environ. Chem. Eng.* **2016**, *5*, 373–380. [CrossRef]
10. Tu, Y.K.; Su, Z.J.; Zhu, Y.X.; Zhang, Y.B.; Xu, J.; Jiang, T. A detoxification and value-added process for chromium ore processing residue (COPR) and Fe-C-bearing dust: Direct reduction-magnetic separation. *Process. Saf. Environ.* **2022**, *167*, 378–389. [CrossRef]
11. Zhao, Q.; Liu, C.J.; Li, B.K.; Zevenhoven, R.; Saxén, H.; Jiang, M.F. Recovery of chromium from residue of sulfuric acid leaching of chromite. *Process. Saf. Environ.* **2018**, *113*, 78–87. [CrossRef]
12. Luo, Z.T.; Zhi, T.Y.; Liu, L.; Mi, J.; Zhang, M.; Tian, C.F.; Si, Z.K.; Liu, X.H.; Mu, Y.D. Solidification/stabilization of chromium slag in red mud-based geopolymer. *Constr. Build. Mater.* **2022**, *316*, 125813. [CrossRef]
13. Song, W.F.; Cao, J.W.; Wang, Z.; Geng, X.H.; Lu, J.S. Glass-ceramics microstructure formation mechanism for simultaneous solidification of chromium and nickel from disassembled waste battery and chromium slag. *J. Hazard. Mater.* **2021**, *403*, 123598. [CrossRef] [PubMed]
14. Ge, X.X.; Zhou, M.K.; Wang, H.D.; Liu, Z.H.; Wu, H.; Chen, X. Preparation and characterization of ceramic foams from chromium slag and coal bottom ash. *Ceram. Int.* **2018**, *44*, 11888–11891. [CrossRef]
15. Wu, Y.W.; Zhai, Y.B. Production practice of chromium slag sintered in Yusteel. *Gansu. Metall.* **2019**, *41*, 101–103. (In Chinese) [CrossRef]

16. Chen, B.J.; Zhou, M.; Jiang, T.; Li, L. Observation of diffusion behavior between Cr_2O_3 and calcium ferrite based on diffusion couple method at 1373 K. *J. Alloys Compd.* **2019**, *802*, 103–111. [CrossRef]

17. Chen, B.J.; Jiang, T.; Zhou, M.; Li, L.; Wen, J.; Wen, Y.C. Interdiffusion kinetics and solid-state reaction mechanism between Cr_2O_3 and calcium ferrite based on diffusion couple method. *J. Alloys Compd.* **2021**, *865*, 158754. [CrossRef]

18. Dang, J. The experiment study on the chromium slag sintering pot. *Jiugang. Technol.* **2020**, *5*, 14–18. (In Chinese)

19. Park, J.; Kim, E.; Suh, I.K.; Lee, J. Effects of basicity and Al_2O_3 content on the crystal structure of silico-ferrite of calcium and aluminum. *ISIJ Int.* **2023**, *63*, 235–243. [CrossRef]

20. Yajima, K.; Jung, S.M. Data arrangement and consideration of evaluation standard for silico-ferrite of calcium and aluminum (SFCA) phase in sintering process. *ISIJ Int.* **2012**, *52*, 535–537. [CrossRef]

21. Ji, Z.Y.; Zhao, Y.J.; Gan, M.; Fan, X.H.; Chen, X.L.; Hu, L. Microstructure and minerals evolution of iron ore sinter: Influence of SiO_2 and Al_2O_3. *Minerals* **2019**, *9*, 449. [CrossRef]

22. Higuchi, K.; Naito, M.; Nakano, M.; Takamoto, Y. Optimization of chemical composition and microstructure of iron ore sinter for low-temperature drip of molten iron with high permeability. *ISIJ Int.* **2004**, *44*, 2057–2066. [CrossRef]

23. Shi, B.J.; Zhu, D.Q.; Pan, J.; Liu, X.Q.; Li, S.W. Combined effect of MgO and basicity varied by different dolomite and burnt lime addition on sintering performance of magnetite concentrates. *Ironmak. Steelmak.* **2019**, *47*, 567–573. [CrossRef]

24. Zhou, M.; Yang, S.T.; Jiang, T.; Xue, X.X. Influence of MgO in form of magnesite on properties and mineralogy of high chromium, vanadium, titanium magnetite sinters. *Ironmak. Steelmak.* **2015**, *42*, 320. [CrossRef]

25. Wang, W.; Yang, D.W.; Ou-Yang, Z.L.; Xu, R.S.; Song, M.M. Effect of SiO_2 on the formation of acicular calcium ferrite in sinter. *Metall. Mater. Trans. B* **2019**, *50*, 678–687. [CrossRef]

26. Yang, D.W.; Wang, W.; Xu, R.S.; Li, J.X.; Song, M.M. Effect of SiO_2 on the mechanical property and reduction of calcium ferrite. *Metals* **2019**, *9*, 152. [CrossRef]

27. Tang, W.D.; Xue, X.X.; Yang, S.T.; Zhang, L.H.; Huang, Z. Influence of basicity and temperature on bonding phase strength, microstructure, and mineralogy of high-chromium vanadium-titanium magnetite. *Int. J. Min. Met. Mater.* **2018**, *25*, 871–880. [CrossRef]

28. Zhang, L.H.; Gao, Z.X.; Yang, S.T.; Tang, W.D.; Xue, X.X. Effect of basicity on sintering behavior and metallurgical properties of high-chromium vanadium-titanium magnetite. *Metals* **2020**, *10*, 569. [CrossRef]

29. Tu, Y.K.; Su, Z.J.; Zhang, Y.B.; Jiang, T. Detoxication and recycling of chromium slag and C-bearing dust via composite agglomeration process (CAP)-blast furnace method. *Waste Manag.* **2023**, *171*, 227–236. [CrossRef] [PubMed]

30. Liu, Y.L.; Liu, T.T.; Pan, F.S. Research progress on intermetallic compounds and solid solutions of Mg alloys based on first-principles calculation. *J. Chongqing Univ.* **2018**, *41*, 30–44. (In Chinese)

31. Bai, J.; Wu, M.; He, Q.; Wang, H.; Liao, Y.; Chen, L.; Chen, S. Emerging doped metal-organic frameworks: Recent progress in synthesis, applications, and first-principles calculations. *Small* **2024**, e2306616. [CrossRef] [PubMed]

32. Hou, M.H.; Jia, L.; Lu, Z.L.; Chen, B.; Kondoh, K.; Cui, J. First-principles study and its experimental verification on the strength and ductility of O/Si solid solution strengthened Ti alloys. *J. Mater. Res. Technol.* **2023**, *27*, 7778–7786. [CrossRef]

33. Roy, I.; Ekuma, C.; Balasubramanian, G. Examining the thermodynamic stability of mixed principal element oxides in AlCoCrFeNi high-entropy alloy by first-principles. *Comput. Mater. Sci.* **2022**, *213*, 111619. [CrossRef]

34. Yang, D.W.; Wang, W.; Li, J.X.; Xu, R.H.; Wang, X.H.; Wang, G. Effect and mechanism of alumina on the morphology and mechanical properties of calcium ferrite. *Metall. Mater. Trans. B* **2020**, *51*, 776–785. [CrossRef]

35. Li, Z.Q.; Zhang, X.; Ma, G.J.; Zheng, D.L.; Xu, J.; Xu, J. Effect of Fe/Cr molar ratio and calcination temperature on preparation of black ceramic pigment with stainless steel dust assisted by microwave processing. *J. Clean. Prod.* **2022**, *372*, 133751. [CrossRef]

36. Tsokov, P.; Blaskov, V.; Klissurski, D.; Tsolovski, I. Effect of mechanical activation on the synthesis of α-Fe_2O_3-Cr_2O_3 solid solutions. *J. Mater. Sci.* **1993**, *28*, 184–188. [CrossRef]

37. Zhang, H.; Shang, S.L.; Wang, Y.; Saengdeejing, A.; Chen, L.Q.; Liu, Z.K. First-principles calculations of the elastic, phonon and thermodynamic properties of $Al_{12}Mg_{12}$. *Acta Mater.* **2010**, *58*, 4012–4018. [CrossRef]

38. Born, M.; Huang, K. *The Dynamical Theory of Crystal Lattices*; Oxford University Press: New York, NY, USA, 1996.

39. Mouhat, F.; Coudert, F.X. Necessary and sufficient elastic stability conditions in various crystal systems. *Phys. Rev. B* **2014**, *90*, 224104. [CrossRef]

40. Chen, K.Y.; Zhao, L.R. Elastic properties, thermal expansion coefficients and electronic structures of $Ti_{0.75}X_{0.5}C$ carbides. *J. Phys. Chem. Solids.* **2007**, *68*, 1805–1811. [CrossRef]

41. Lou, Y.R. *Comprehensive Handbook of Chemical Bond Energies*; CRP Press: New York, NY, USA, 2007.

42. Hu, T.H.; Li, Z.H.; Zhang, Q.F. First principles and molecular dynamics simulations of effect of dopants on properties of high strength steel for hydrogen storage vessels. *Acta Phys. Sin.* **2024**, *73*, 067101. (In Chinese) [CrossRef]

43. Ye, T.Z.; Wang, Z.T.; Wu, Y.W.; Zhang, J.; Chen, P.; Wang, M.J.; Tian, W.X.; Su, G.H.; Qiu, S.Z. Molecular dynamics simulation of tensile deformation behavior of single-crystal Fe-Cr-Al before and after irradiation. *J. Mater. Res.* **2022**, *38*, 828–840. [CrossRef]

44. Wei, X.; Chen, Z.G.; Zhong, J.; Wang, L.; Wang, Y.P.; Shu, Z.L. First-principles investigation of Cr-doped Fe_2B: Structural, mechanical, electronic and magnetic properties. *J. Magn. Magn. Mater.* **2018**, *456*, 150–159. [CrossRef]

45. Pugh, S.F. XCII. Relations between the elastic moduli and the plastic properties of polycrystalline pure metals. *Philos. Mag.* **1954**, *45*, 823–843. [CrossRef]

46. Zhang, D.X.; Wang, J.; Dong, K.Z.; Hao, A.M. First principles investigation on the elastic and electronic properties of Mn, Co, Nb, Mo doped $LiFePO_4$. *Comput. Mater. Sci.* **2018**, *155*, 410–415. [CrossRef]

47. Tu, Y.K.; Zhang, Y.B.; Su, Z.J.; Jiang, T. Mineralization mechanism of limonitic laterite sinter under different fuel dosage: Effect of FeO. *Powder Technol.* **2022**, *398*, 117064. [CrossRef]

48. Xue, Y.X.; Pan, J.; Zhu, D.Q.; Guo, Z.Q.; Tian, H.Y.; Shi, Y.; Lu, S.H. Effect of alumina occurrence on sintering performance of iron ores and its action mechanism. *J. Mater. Res. Technol.* **2021**, *12*, 1157–1170. [CrossRef]

49. Xu, J.; Ma, G.J.; Zheng, D.L.; Zhang, X.; Hai, Y.H. Influence of chromium slag on the microstructure and metallurgical performance of sinter. *Sinter. Pelletiz.* **2023**, *48*, 16–23. (In Chinese)

50. Wu, H.; Huang, S.R.; Zhu, C.Y.; Zhu, H.G.; Xie, Z.H. Influence of Cr content on the microstructure and mechanical properties of $Cr_xFeNiCu$ high entropy alloys. *Prog. Nat. Sci.* **2020**, *30*, 239–245. [CrossRef]

51. Liu, Y.; Fang, C.X.; Lin, S.H.; Liu, G.H.; Zhang, B.H.; Shi, H.H.; Dong, N.; Yang, N.X.; Zhang, F.C.; Guo, X.; et al. Calculation of mechanical properties, electronic structure and optical properties of $CsPbX_3$ (X = F, Cl, Br, I). *Molecules* **2023**, *28*, 7643. [CrossRef] [PubMed]

52. Wang, D.T.; Zhang, X.Z.; Nagaumi, H.M.; Zhang, M.H.; Zhou, P.F.; Wang, R.; Zhang, B. Exploring the relationship between the structural characteristics and mechanical behavior of multicomponent Fe-containing phases: Experimental studies and first-principles calculations. *Molecules* **2023**, *28*, 7141. [CrossRef]

53. Hamilton, J.D.G.; Hoskins, B.F.; Mumme, W.G.; Borbidge, W.E.; Montague, M.A. The crystal structure and crystal chemistry of $Ca_{2.3}Mg_{0.8}Al_{1.5}Si_{1.1}Fe_{8.3}O_{20}$ (SFCA): Solid solution limits and selected phase relationships of SFCA in the SiO_2-Fe_2O_3-CaO(-Al_2O_3). *Neues. Jahrb. Für. Mineral. Abhandlungen.* **1989**, *161*, 1–26.